

Transverse and Axial Resolution of Femtosecond Laser Surgery

Yao L. Wang

Northeastern University

Noa W. F. Grooms

Northeastern University

Samuel H. Chung (✉ schung@northeastern.edu)

Northeastern University

Research Article

Keywords: pulsed laser, femtosecond laser, laser surgery, transverse resolution, axial resolution, *Caenorhabditis elegans*, regeneration

Posted Date: April 13th, 2021

DOI: <https://doi.org/10.21203/rs.3.rs-406760/v1>

License:  This work is licensed under a Creative Commons Attribution 4.0 International License.

[Read Full License](#)

1 **Title page**
2

3 **Title:**

4 Transverse and axial resolution of femtosecond laser surgery
5

6 **Running title:**

7 Axial resolution of laser surgery
8

9 **Author names and affiliations:**

10 Yao L. Wang^{1◊}, Noa W. F. Grooms^{1◊}, Samuel H. Chung^{1*}
11 [◊]equal contribution

12 ¹Department of Bioengineering, Northeastern University, Boston, Massachusetts, USA
13

14 *Corresponding author

15 E-mail: schung@northeastern.edu
16

17 **Keywords:** pulsed laser, femtosecond laser, laser surgery, transverse resolution, axial
18 resolution, *Caenorhabditis elegans*, regeneration
19

20 **Author contributions:**

21 Several people contributed to the work described in this paper. SHC conceived the idea.
22 YLW and NWFG carried out experiments, and all authors analyzed the data. SHC
23 supervised the experiments and the development of the manuscript. SHC wrote the first
24 draft of the manuscript; all authors subsequently took part in the revision process and
25 approve the final copy of the manuscript.

26 Abstract

27 Femtosecond lasers are capable of precise ablation inside transparent media, including
28 glass and *in vivo* samples. The transverse and axial resolution of damage inside the bulk
29 are important parameters of ablation. The transverse resolution is straightforward to
30 measure, but the axial resolution is much more difficult to measure and rarely performed.
31 Using a 1040-nm, 400-fs pulsed laser, we performed ablation inside glass with a
32 transverse and axial resolution of 0.75 m. By fitting damage spot measurements to
33 theoretical predictions, we find an ablation threshold of $6.4 \times 10^{12} \text{ W/cm}^2$. We also ablated
34 neuron cell bodies and fibers in *C. elegans* and demonstrate submicrometer resolution in
35 both the transverse and axial directions, consistent with our results in glass. Using simple
36 yet rigorous methods, we define the resolution of laser ablation in transparent media
37 along all directions.

38 Introduction

39 The advent of the laser in 1960¹ was immediately followed by its application for surgery
40 in a variety of research and medical samples (reviewed in Ref. [2]). Scientists and
41 clinicians recognized that focused laser light can produce highly confined damage to
42 materials, resulting in dissection with resolution unachievable through conventional
43 means. The sample absorbs laser light, acquiring sufficient energy to vaporize the
44 material. Laser surgery (or ablation) can be roughly divided into two regimes based on
45 location: superficial and bulk. In the superficial regime, laser pulses impinge on a surface,
46 leading to explosive removal of material from the surface. Surgery in the bulk requires
47 laser light to penetrate through the sample to its target. To permit propagation of any
48 appreciable distance, the sample must be relatively transparent to the laser wavelength.
49 Absorption of laser light in the bulk is typically achieved by focusing the laser beam on
50 the target and thereby greatly increasing linear absorption or stimulating nonlinear
51 absorption. Depending on the amount of laser energy deposited, the laser generates low
52 to high-density plasma, leading to damage and, at higher energies, an explosion and
53 shockwaves generating damage beyond the focal volume.

54 A steadily growing number of studies have characterized laser surgery of biological
55 samples. As biological media are primarily composed of water, the foundational studies
56 on ablation in water apply to biological surgery. Moreover, the mechanisms of laser
57 propagation, laser absorption, and material vaporization are similar between many
58 transparent materials. Thus, studies performed on various glasses and transparent
59 semiconductors are also relevant to understanding the processes of laser surgery on
60 biological media. Based on extensive prior studies in ablation of transparent material, a

61 key parameter for laser surgery is the intensity threshold for nonlinear absorption. An
62 intensity above the threshold triggers nonlinear absorption, and energy transfers into the
63 material³. Together with the parameters for laser focusing, the intensity threshold sets a
64 focal volume where the laser pulses can vaporize material and cause damage.

65 To some degree, laser surgery (input of light into the sample) is imaging (output of
66 light from sample) in reverse. Many of the same optical mechanisms apply, including
67 some of the calculations for resolution. In recent years, there has been a proliferation of
68 lasers for surgery as well as new techniques for imaging. While assessing the transverse
69 resolution of a technique is a requirement of establishing it, significantly fewer studies
70 assess the axial, or longitudinal, resolution of imaging or surgery. This is partially due to
71 the physical challenges of imaging along a direction orthogonal to the optical axis. Prior
72 studies have gained optical access to side-views through several methods: In one study,
73 an ablated piece of glass was polished down to access the damage spot⁴. Other studies
74 fractured the glass and then imaged it with brightfield, differential interference contrast
75 microscopy, or scanning electron microscopy following graphite coating^{5,6}. Another study
76 used two objectives to image from the side while ablating⁷, and a recent study physically
77 cut a soft sample with a razor blade to expose the damaged spot⁸.

78 Given the importance of imaging and surgery resolution in the axial direction, we seek
79 to establish rigorous techniques for assessing it. In a prior study we established a
80 technique to measure the illumination resolution of widefield and scanned microscopy⁹.
81 Here, we first measure resolution of laser ablation in glass and use simple mathematical
82 relationships to calculate the threshold intensity and the minimum focal region. Second,
83 we also measure damage sizes *in vivo* in the transverse and axial directions to establish

84 the resolution. Third, we present one piece of evidence suggesting that fibers are not
85 damaged by ablation outside of the axial damage region.

86

87 **Results**

88 Our setup is shown in Fig. 1a. A femtosecond laser outputs 1040-nm 400-fs pulses which
89 we expand and send into a 1.4 numerical aperture (NA), 60x microscope objective. In our
90 biological samples, we image epifluorescently through the same objective. We input
91 illumination light and image fluorescent light from the sample onto an array camera.

92

93 Theoretical considerations

94 This section derives the transverse (xy) and axial (z) intensity distributions for a focused
95 beam propagating in the z direction in a homogeneous medium. We partially follow the
96 derivation in Chapter 2.5 of Ref. [10] with adjustments to follow the derivation in Ref. [11].
97 We utilize the final results to model and determine the damage spot dimensions in the
98 sections below¹².

99 In brief, laser pulses can be modeled by beams whose intensity distribution is
100 Gaussian in the transverse direction. Because of diffraction, focused beams come to a
101 minimum width called the waist, at the focal plane (see Fig. S1). The intensity distribution
102 is Lorentzian in the axial direction, and the beam width is hyperboloid in the axial direction,
103 as shown in Fig. S1. The intensity is $I = P / A = P / r^2$, where I , P , A , and r are the optical
104 intensity, optical power, beam cross-sectional area, and beam radius, respectively.
105 Specifically,

106

$$I(x, y, z) = \frac{P_0}{\pi\omega^2(z)} e^{-\frac{x^2+y^2}{\omega^2(z)}}.$$

107 where P_0 is the peak power level and $\omega^2(z) = \omega_0^2 \left[1 + \frac{z^2}{z_0^2} \right]$ is the squared radius of the
 108 beam. ω_0 is the beam waist radius at $1/e^2$ intensity. z_0 is the Rayleigh range ($2z_0$ is also
 109 known as the confocal parameter), or the distance from the waist where the intensity
 110 drops by half ¹⁰. Note that, intuitively, the total power at each axial position must be
 111 constant if there is no absorption or scattering. Confirming this, the total power is the
 112 integral of $I(x, y, z)$ over the transverse directions, which yields the peak power, P_0 .

113

114 We consider simple beams with azimuthal symmetry, so $r^2 = x^2 + y^2$ and

115

$$I(r, z) = \frac{P_0}{\pi\omega^2(z)} e^{-\frac{r^2}{\omega^2(z)}}.$$

116 Thus, at the waist ($z = 0$) the intensity is

117

$$I(r, 0) = \frac{P_0}{\pi\omega_0^2} e^{-\frac{r^2}{\omega_0^2}}.$$

118 Along the optical axis ($r = 0$) the intensity is

119

$$I(0, z) = \frac{P_0}{\pi\omega^2(z)} = \frac{P_0}{\pi\omega_0^2} \frac{1}{1 + z^2/z_0^2}.$$

120 Absorption of laser beams in nominally transparent materials occurs if the laser intensity
 121 exceeds a threshold, I_{th} , dependent on the optical properties of the material³. The laser
 122 intensity distribution is peaked in the transverse and axial directions. For a given laser
 123 power, the intensity meets the threshold at defined transverse r_{th} or axial z_{th} radii, where

124

125
$$I(r_{th}, 0) = \frac{P_0}{\pi\omega_0^2} e^{-\frac{r_{th}^2}{\omega_0^2}} = I_{th}$$

126 or

127
$$I(0, z_{th}) = \frac{P_0}{\pi\omega_0^2} \frac{1}{1 + z_{th}^2/z_0^2} = I_{th}.$$

128 Within this r_{th} or z_{th} , material can be ionized by the laser, forming a damage spot.

129 The pulse energy, E , is the time integral of $P(t)$, the time evolution of a single pulse's
130 power. Assuming a Gaussian shape in time, $P_0 = \sqrt{\frac{4 \ln 2}{\pi}} E/\tau = 0.94 E/\tau$, where $\tau = 400$

131 fs is the pulse duration¹³. The average laser power is $P_{avg} = E * f_{rep}$, where $f_{rep} = 1$ kHz
132 is the repetition rate. Thus, the respective sizes of the damage spot in the transverse and
133 axial directions are

134
$$r_{th}(P_{avg}) = \omega_0 \sqrt{\ln \frac{P_0}{\pi\omega_0^2 I_{th}}} = \omega_0 \sqrt{\ln \frac{0.94 P_{avg}}{\tau f_{rep} \pi \omega_0^2 I_{th}}} \quad \text{Eq. 1}$$

135 and

136
$$z_{th}(P_{avg}) = z_0 \sqrt{\frac{P_0}{\pi\omega_0^2 I_{th}} - 1} = z_0 \sqrt{\frac{0.94 P_{avg}}{\tau f_{rep} \pi \omega_0^2 I_{th}} - 1}. \quad \text{Eq. 2}$$

137

138 Glass ablation

139 The resolution of laser surgery in biological media is relatively difficult to assess. The
140 media itself is often heterogeneous, complicating observation of surgical alterations.
141 Following surgery, damage locations are rapidly flooded with water from surrounding
142 tissues, reducing index differences, contrast with the background, and visibility. One
143 simple method for assessing resolution is to ablate glass, as shown in Fig. 1b. Ablation
144 of glass with pulses of greater intensity than the threshold leads to permanent material

145 changes, including an increase in the refractive index that allows measurement of the
146 damage size¹⁴. Measuring transverse sizes of the damage spot at various pulse energies
147 is simply a matter of ablating and imaging in the same location. Measuring the axial size
148 of the damage spot is significantly more difficult. As shown in Fig. 1b, after ablating a
149 polished block of glass near a corner, we rotated the block of glass 90° to image the
150 damage spot in the orthogonal direction (*i.e.*, *xz*). We fill gaps between the objective,
151 coverslip, and the glass block with index matching fluid (blue). The fluid ensures that
152 ablation and imaging light encounters a constant refractive index, which maximizes light
153 transmission and minimizes optical distortion,

154 We empirically determined the absorption threshold under our setup (see Materials
155 and methods) to be 50 W average power at 1 kHz repetition rate, or 50 nJ pulse energy.
156 Surprisingly, near the threshold the spot dimensions in transverse and axial directions
157 were very similar, about 0.75 m diameter. As the pulse energy increased, the axial extent
158 of the damage spot increased more rapidly than the transverse, as expected from Eqs.
159 1-2. In the section above, we derive the equations governing the intensity distribution in
160 the transverse and axial directions. The transverse dimensions obey a Gaussian
161 distribution while the axial dimensions obey a Lorentzian distribution. We ablated N-BK7
162 glass with 50-90 W of power, producing damage spots of various diameters in *x*, *y*, and
163 *z* (see Fig. 2a). Fitting the damage spot measurements to Eq. 1 by MATLAB, we obtain
164 transverse waist radius σ_0 of 0.67 m and an intensity threshold I_{th} of $6.3 \times 10^{12} \text{ W/cm}^2$
165 (see Fig. 2b, Tab. 1). As described in the methods, we utilized the average σ_0 from the *x*
166 and *y* fits for modeling the axial damage spot size. Fitting the damage spot measurements

167 to Eq. 2, we obtain a Rayleigh range z_0 of 0.69 m and an intensity threshold I_{th} of 6.5 \square
 168 10^{12} W/cm^2 (see Fig. 2b, Tab. 1).

169

170 Table 1

	x	y	z
σ (m)	0.66	0.68	
z_0 (m)			0.69
I_{th} (W/cm ²)	6.5×10^{12}	6.0×10^{12}	6.5×10^{12}

171

172

173 *In vivo* ablation

174 We also characterized the transverse and axial resolution of our surgeries *in vivo* on
 175 neurons in *C. elegans*. First, following prior studies^{12,15}, we demonstrated transverse
 176 resolution by ablating the middle fiber in a tight bundle of dendrites. The first ablation in
 177 Fig. 3a (after #1) shows a cut of resolution better than 1.03 m. The second ablation (after
 178 #2) shows a cut of resolution better than 0.75 m. The first cut widens between the “after
 179 #1” and the “after #2” images due to dendrite tension. These data indicate an *in vivo*
 180 transverse resolution of well below 1 m, a similar resolution to our prior work using 800-
 181 nm Ti:sapphire and 1030-nm Yb-doped fiber lasers^{12,15}.

182 Second, in multiple studies, we have ablated cell bodies for several seconds to kill off
 183 entire cells^{15,16}. We visualize and target single cells by a diffusible cell-specific green
 184 fluorescent protein (GFP) labelling the entire cell. In the early stages of cell body ablation,

185 we often find that the cell body's nucleus dims while the cytoplasm remains fluorescent
186 (see Fig. 3b). This dimming occurs because the nuclear GFP diffuses to the laser focus
187 and is selectively ablated and photobleached. Laser ablation spares the nuclear
188 membrane, which prevents the diffusion of cytoplasmic GFP and photobleaching of the
189 entire cell. As shown in Fig. 3b, irradiating the bright nucleolus (arrow) leads to dimming
190 of the entire nucleus but not the cell cytoplasm. Thus, we have long known that the axial
191 resolution of laser ablation is far below 2 μm, the axial width of the nucleus.

192 Third, to further define the axial resolution, we focused laser pulses at specific
193 locations below, directly on, or above single dendrites. As shown in Fig. 3c, ablating at
194 the fiber axial position severs the fiber while ablating a sufficient distance above or below
195 the fiber does not sever the fiber. We tracked the percentage of fibers severed by focusing
196 at each depth relative to the fiber's axial position. As shown in Fig. 3d, the efficacy of laser
197 surgery peaks when the laser pulses are focused on or near (≤ 0.2 μm) the fiber. Surgical
198 efficacy decreases roughly symmetrically as the focus moves away from the fiber. At
199 approximately ± 0.4 - 0.5 μm there is a clear transition from severing to non-severing. Laser
200 pulses focused at 0.75 μm away from the fiber or further are unable to sever the fiber.
201 There is noticeable pulse-to-pulse variability in the laser's operation. Sequential pulses
202 can focus on slightly different transverse and axial positions over a range of ~0.1-0.2 μm.
203 Thus, these data indicate that the axial resolution of laser surgery is slightly below 1 μm.

204 Lastly, to determine if invisible dendrite damage could occur without severing the
205 dendrite, we cut neurites in the ASJ neuron and noted axon regeneration after surgery.
206 Worms regenerate axons robustly under multiple mechanisms¹⁷. In mutants with
207 defective dual-leucine zipper kinase, denoted as *dlk-1*, multiple neuron types have

208 severely reduced axon regeneration¹⁸. The ASJ axon shows no regeneration in *dlk-1*
209 when it is the sole fiber cut; however, the ASJ neuron exhibits a “conditioned” form of
210 regeneration when the sensory dendrite is also severed. Nearly 100% of ASJ axons
211 regenerate in *dlk-1* if both the axon and dendrite are severed¹⁷. For a given neuron in the
212 *dlk-1* background, we cut its axon by ablating directly on the axon and then ablated at
213 various depths relative to the dendrite. As expected, *dlk-1* animals with only axon cuts
214 showed no regeneration. When we ablate directly on the dendrite, the axon regenerates
215 on average 10.3 ± 9.7 m. When the dendrite is ablated 0.5 m above or below its depth
216 without severing it, there is essentially no regeneration. These data further confirm the
217 tight confinement of laser damage to the focal plane.

218

219 **Discussion**

220 While both the transverse and axial resolution are needed to fully characterize laser
221 surgery, the axial resolution is rarely measured. Here we determine the transverse and
222 axial resolution of a Yb-doped diode-pumped solid-state femtosecond laser by ablating a
223 transparent material and *in vivo* biological samples. By solving the Gaussian and
224 Lorentzian intensity distributions for r_{th} and z_{th} (see Theoretical considerations), we find
225 that the transverse radius of ablation is proportional to the square root of the natural
226 log of P_{avg} , while the axial radius of ablation is proportional to the square root of P_{avg} . By
227 ablating glass at various powers, directly measuring the damage spot in all three
228 dimensions, and fitting the measurements to the equations derived, we find an intensity
229 threshold of $6.4 \times 10^{12} \text{ W/cm}^2$ for glass ablation. Our results are roughly consistent with

230 prior studies showing intensity thresholds of $8 - 20 \times 10^{12} \text{ W/cm}^2$ of various glasses under
231 femtosecond pulses of different wavelengths and pulse durations (e.g., [19,20]).
232 Importantly, we demonstrate that the minimum focal region radii and the damage radii
233 near the threshold differ by less than 3% in the transverse and axial directions (Fig. 2b).

234 We also characterized the resolution of 1040-nm femtosecond laser surgery in *C.*
235 *elegans* neurons *in vivo*. Similar to our prior studies utilizing 800-nm pulses¹⁵, we show a
236 transverse resolution that is submicrometer. Likewise, we show an axial resolution that is
237 also submicrometer. Note that even though the laser pulses pass through the fibers (Fig.
238 3c), they do not damage them unless the region where the laser intensity exceeds the
239 threshold impinges on the fiber. It is only in this region that laser light is absorbed and
240 damage occurs. Finally, we also tested for invisible damage by assaying if conditioned
241 regeneration occurs by ablating at 0.5 m above and below the dendrite and directly at
242 the dendrite. We found that ablation directly on the dendrite is necessary to trigger
243 regeneration, consistent with a submicrometer axial resolution of laser surgery.

244 To our knowledge, our study is one of only a few studies that examine the axial
245 resolution of laser ablation in transparent media. Even fewer studies examine the axial
246 resolution of laser surgery in biological samples. An increasing number of studies utilize
247 laser surgery in biological contexts. Thus, rigorously defining its resolution in all three
248 dimensions is crucial for understanding its capacity for creating high-precision dissections
249 without collateral damage.

250 **Materials and methods**

251 **Microscope setup:** We utilized a Nikon Ti2-E inverted microscope with a SOLA SE II
252 LED light engine to take 3D image stacks. We used a 1.4 NA, 60x objective for ablation
253 and imaging.

254 **Laser setup:** A Yb-doped diode-pumped solid-state laser (SpectraPhysics Spirit-
255 1040-4W) outputs 1040-nm 400-fs pulses with a repetition rate of 1 kHz. As shown in Fig.
256 1a, we expanded the diameter of the laser beam through a 10x beam expander (Thorlabs
257 GBE10-B) to overfill the back aperture of our microscope objective. We raised the beam
258 using a custom periscope (not shown) to send into the upper turret of a Nikon Ti2-E
259 epifluorescence inverted microscope. A mechanical shutter in the upper turret controls
260 the laser irradiation. We illuminated through the lower turret, typically with blue light, and
261 the emission light was imaged by an sCMOS camera (Andor Zyla 4.2).

262 **Glass ablation and damage spot characterization:** As shown in Fig. 1b, we
263 performed all glass ablation on an N-BK7 block of glass polished to 20-10 scratch-dig.
264 Two faces on this block form a right angle. We attached a coverslip with immersion oil
265 onto one face. We added objective immersion oil to all the locations that transmit the
266 illumination or laser beam. This prevents impinging of illumination or laser light on a low-
267 index region possibly leading to reflection rather than transmission. We acquired the
268 damage spot xy images by brightfield imaging through the same face as laser
269 transmission. For xz imaging of the laser damage spot, after laser ablation through one
270 face, we separated the glass block from the coverslip. We then rotated the glass block by
271 90° and repeated the same process of attaching the coverslip and imaging on the
272 orthogonal face. Ablation of glass creates a damage spot that refracts light and is evident

273 in brightfield images. In ImageJ, we measured the size of a damage spot using the
274 intensity profile of a line through the center of the spot. We defined the size to be the inner
275 diameter of the spot, where the intensity profile intersects the background value. By
276 MATLAB, we utilized these sizes together with the average laser power to fit Eqs. 1-2 and
277 determine the minimum spot σ_0 , z_0 , and the intensity threshold.

278 **In vivo ablation:** We followed preoperative procedures established for laser
279 microsurgery in *C. elegans*^{15,21}. Animals carried fluorescently-labeled ASJ neurons. We
280 mounted young adults onto sodium azide agarose pads for immobilization. We followed
281 established procedures to sever the ASJ dendrite^{3,15}. To characterize the transverse
282 resolution of laser damage, we severed tightly-bundled fibers in the amphid dendrite
283 bundle (Fig. 3a). We measured the gap between unsevered fibers using ImageJ. For
284 characterizing axial resolution, we aimed our laser at the ASJ nucleolus and ablated it for
285 several seconds (Fig. 3b), following established protocol¹⁵. We also ablated at defined
286 locations above or below the dendrite (Fig. 3cd) and noted percentage of successful
287 severing.

288 **Regeneration characterization:** We followed procedures previously established in
289 our laboratory for studying regeneration¹⁷. In young adult aged worms we severed the
290 axon, the axon and ipsilateral dendrite, or the axon and then ablated 0.5 m above or
291 below the ipsilateral dendrite without severing (Fig. 4ab). We followed postoperative
292 procedures to recover worms in nematode growth medium and continued cultivation at
293 20°C. We reimaged worms 48 hours post-surgery. We measured the length of
294 regeneration in ImageJ by using the 3D Distance Tool plugin available at the NIH ImageJ
295 website following established procedures¹⁷.

296 **C. elegans cultivation, immobilization, imaging:** We followed established
297 procedure for *C. elegans* strains cultivation on agar plates²² at 15 or 20 °C, animal
298 immobilization by sodium azide, and imaging¹⁵. After immobilization, animals were
299 rotated to a desired orientation³ under a fluorescence stereomicroscope and then imaged
300 under an inverted microscope.

301 **C. elegans strains:** We used the following strains for this study: *dik-1(ju476)I*;
302 *ofls1[lin-15ab+; trx-1::gfp]IV*, *tax-2(p691)I*; *ofls1[lin-15ab+; trx-1::gfp]IV*, and NG3146
303 *gmls18[ceh-23::gfp; rol-6]X*.

304 **Statistics and interpretation of results:** We calculated *p*-values for frequency of
305 successful cuts with the Fisher's exact test. We calculated *p*-values for regenerated
306 length measurements by the unpaired, unequal variance, two tailed *t*-test.

307 **Acknowledgements**

308 We thank the members of the Chung Laboratory for feedback on the manuscript. NG3146
 309 is a gift from Gian Garriga.
 310

311

312 **References**

- 313 1 Maiman, T. H. Stimulated Optical Radiation in Ruby. *Nature* **187**, 493-494 (1960).
- 314 2 Chung, S. H. & Mazur, E. Surgical applications of femtosecond lasers. *Journal of*
 315 *Biophotonics* **2**, 557-572 (2009).
- 316 3 Chung, S. H. & Mazur, E. Femtosecond laser ablation of neurons in C. elegans for
 317 behavioral studies. *Appl. Phys. A-Mater. Sci. Process.* **96**, 335-341,
 318 doi:10.1007/s00339-009-5201-7 (2009).
- 319 4 Glezer, E. N. *et al.* Three-dimensional optical storage inside transparent materials.
 320 *Opt. Lett.* **21**, 2023-2025, doi:10.1364/OL.21.002023 (1996).
- 321 5 Schaffer, C. B., Brodeur, A., Garcia, A. F. & Mazur, E. Micromachining bulk glass
 322 by use of femtosecond laser pulses with nanojoule energy. *Opt. Lett.* **26**, 93-95
 323 (2001).
- 324 6 Schaffer, C. B., Jamison, A. O. & Mazur, E. Morphology of femtosecond laser-
 325 induced structural changes in bulk transparent materials. *Appl. Phys. Lett.* **84**,
 326 1441-1443, doi:10.1063/1.1650876 (2004).
- 327 7 Watanabe, W. & Itoh, K. Motion of bubble in solid by femtosecond laser pulses.
 328 *Opt. Express* **10**, 603-608, doi:10.1364/OE.10.000603 (2002).
- 329 8 Saerchen, E. *et al.* Femtosecond laser induced step-like structures inside
 330 transparent hydrogel due to laser induced threshold reduction. *PLOS ONE* **14**, 15,
 331 doi:10.1371/journal.pone.0222293 (2019).
- 332 9 Wang, Y. L., Grooms, N. W. F., Civale, S. C. & Chung, S. H. Confocal imaging
 333 capacity on a widefield microscope using a spatial light modulator. *PLOS ONE* **16**,
 334 e0244034, doi:10.1371/journal.pone.0244034 (2021).
- 335 10 Yariv, A. *Optical Electronics in Modern Communications.* (Oxford University
 336 Press, 1997).

- 337 11 Liu, J. M. Simple technique for measurements of pulsed Gaussian-beam spot
338 sizes. *Opt. Lett.* **7**, 196-198, doi:10.1364/OL.7.000196 (1982).
- 339 12 Harreguy, M. B. *et al.* Ytterbium-doped fibre femtosecond laser offers robust
340 operation with deep and precise microsurgery of *C. elegans* neurons. *Sci. Rep.* **10**,
341 4545, doi:10.1038/s41598-020-61479-0 (2020).
- 342 13 Paschotta, R. *Field Guide to Laser Pulse Generation*. (Society of Photo Optical,
343 2008).
- 344 14 Schaffer, C. B., Garcia, J. F. & Mazur, E. Bulk heating of transparent materials
345 using a high repetition-rate femtosecond laser. *Appl. Phys. A-Mater. Sci. Process.*
346 **76**, 351-354 (2003).
- 347 15 Chung, S. H., Clark, D. A., Gabel, C. V., Mazur, E. & Samuel, A. D. The role of the
348 AFD neuron in *C. elegans* thermotaxis analyzed using femtosecond laser ablation.
349 *BMC Neurosci.* **7**, 30 (2006).
- 350 16 Chung, S. H., Schmalz, A., Ruiz, R. C. H., Gabel, C. V. & Mazur, E. Femtosecond
351 Laser Ablation Reveals Antagonistic Sensory and Neuroendocrine Signaling that
352 Underlie *C-elegans* Behavior and Development. *Cell Reports* **4**, 316-326,
353 doi:10.1016/j.celrep.2013.06.027 (2013).
- 354 17 Chung, S. H. *et al.* Novel DLK-independent neuronal regeneration in
355 *Caenorhabditis elegans* shares links with activity-dependent ectopic outgrowth.
356 *Proc. Natl. Acad. Sci. USA* **113**, E2852-E2860, doi:10.1073/pnas.1600564113
357 (2016).
- 358 18 Hammarlund, M., Nix, P., Hauth, L., Jorgensen, E. M. & Bastiani, M. Axon
359 Regeneration Requires a Conserved MAP Kinase Pathway. *Science* **323**, 802-806
360 (2009).
- 361 19 Stuart, B. C., Feit, M. D., Rubenchik, A. M., Shore, B. W. & Perry, M. D. Laser-
362 Induced Damage in Dielectrics with Nanosecond to Subpicosecond Pulses. *Phys.*
363 *Rev. Lett.* **74**, 2248-2251 (1995).
- 364 20 Lebugle, M., Sanner, N., Utéza, O. & Sentis, M. Guidelines for efficient direct
365 ablation of dielectrics with single femtosecond pulses. *Appl. Phys. A* **114**, 129-142,
366 doi:10.1007/s00339-013-8153-x (2014).
- 367 21 Bargmann, C. I. & Avery, L. Laser killing of cells in *Caenorhabditis elegans*.
368 *Methods Cell Biol.* **48**, 225-250 (1995).
- 369 22 Brenner, S. The genetics of *Caenorhabditis elegans*. *Genetics* **77**, 71-94 (1974).

370

371

372

373 **Figure captions**374 **Figure 1. Ablation and imaging setup.** (a) Microscope setup for ablation and imaging.

375 1040-nm femtosecond laser beam is expanded and focused on sample by objective.

376 Illumination light is focused by same objective, and emission light is imaged onto array

377 camera by tube lens. (b) Procedure for axial (*xz*) plane imaging. Glass block is ablated

378 near edge by laser, rotated 90°, and imaged. Gaps in beampath are filled with immersion

379 oil (blue) to homogenize refractive index.

380

381 **Figure 2. Glass damage spots match theoretical predictions.** (a) Transverse and axial

382 plane images of glass damage by focused laser pulses of 50-90 W. (b) Damage spot

383 measurements in *x* (diamond), *y* (square), and *z* (circle) directions. Green and orange384 curves plot Eq. 1 with best fit z_0 and I_{th} . Black curve plots Eq. 2 with best fit z_0 and I_{th} .

385

386 **Figure 3. Characterization of *in vivo* laser surgery.** (a) Individual neuronal fibers in387 tight bundle before, after 1st ablation, after 2nd ablation. Images indicate submicrometer

388 transverse resolution of laser surgery. (b) Ablation and photobleaching of nucleus but not

389 cytoplasm shows persistence of nuclear membrane, suggesting axial resolution well

390 below 2 m. (c) Fiber severed by ablation directly at its axial position but spared by

391 ablation 0.75 m above or below fiber. (d) Percentage of fibers severed by ablation at

392 various axial positions relative to the fiber. Results indicate submicrometer axial resolution
393 of laser surgery.

394

395 **Figure 4. Regeneration assay confirms submicrometer resolution of laser surgery.**

396 (a) Line drawings and fluorescent images of ASJ neuron. Control (left) neuron with intact
397 dendrite (black) and axon (gray). Non-control images taken 2 days after surgery:
398 Postsurgery neuron (middle) with cut axon and ablation 0.5 m below dendrite. Axon has
399 decayed away. Postsurgery neuron (right) with regenerated axon and dendrite ablated
400 directly at its axial position. (b) Length regenerated for each axon cut. Significant
401 regeneration only occurs when dendrites are ablated directly at their axial position;
402 Average and standard deviation indicated by bars. Triangles pointed in direction of side
403 cut. ** $p < 0.0005$.

Figures

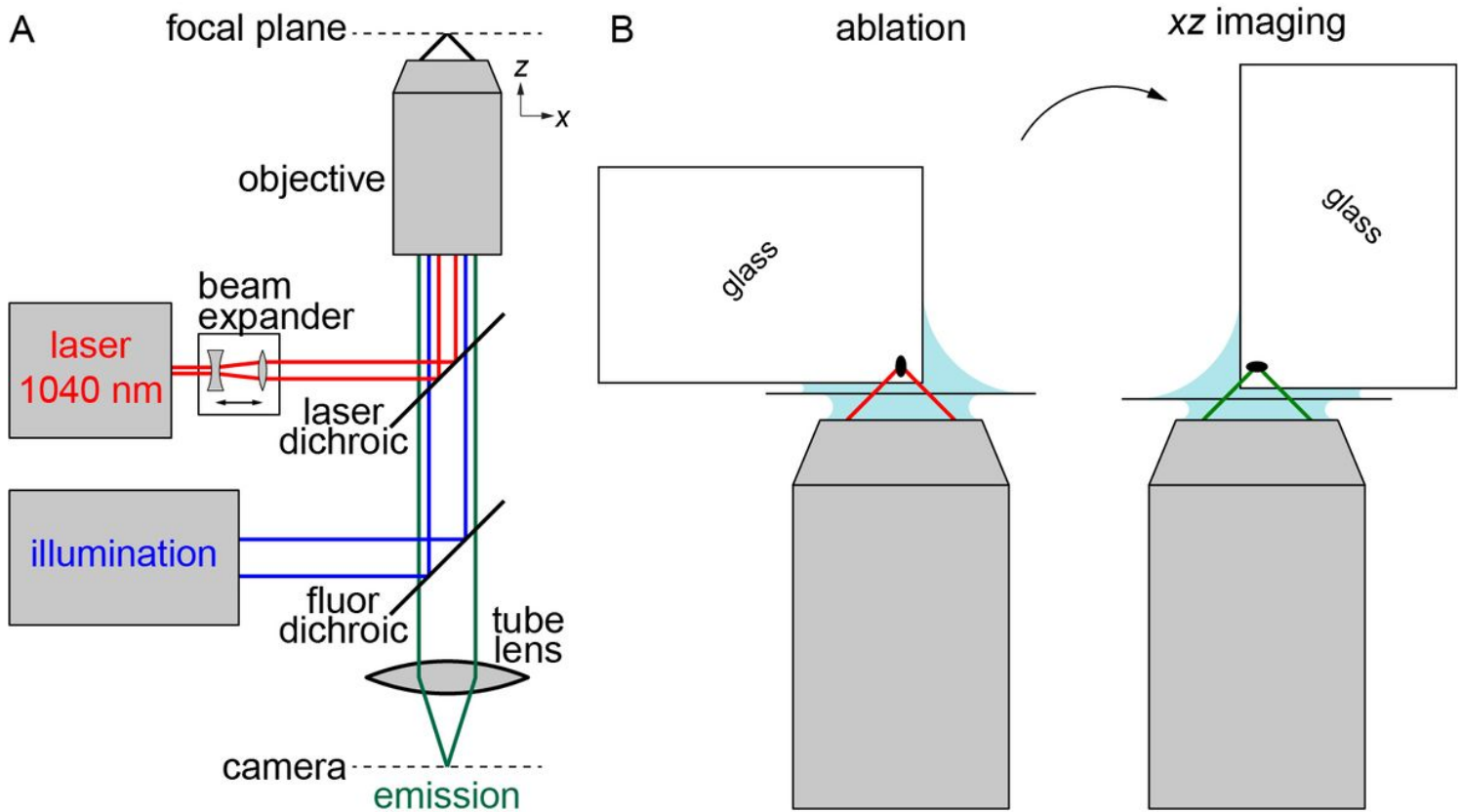


Figure 1

Ablation and imaging setup. (a) Microscope setup for ablation and imaging. 1040-nm femtosecond laser beam is expanded and focused on sample by objective. Illumination light is focused by same objective, and emission light is imaged onto array camera by tube lens. (b) Procedure for axial (xz) plane imaging. Glass block is ablated near edge by laser, rotated 90°, and imaged. Gaps in beampath are filled with immersion oil (blue) to homogenize refractive index.

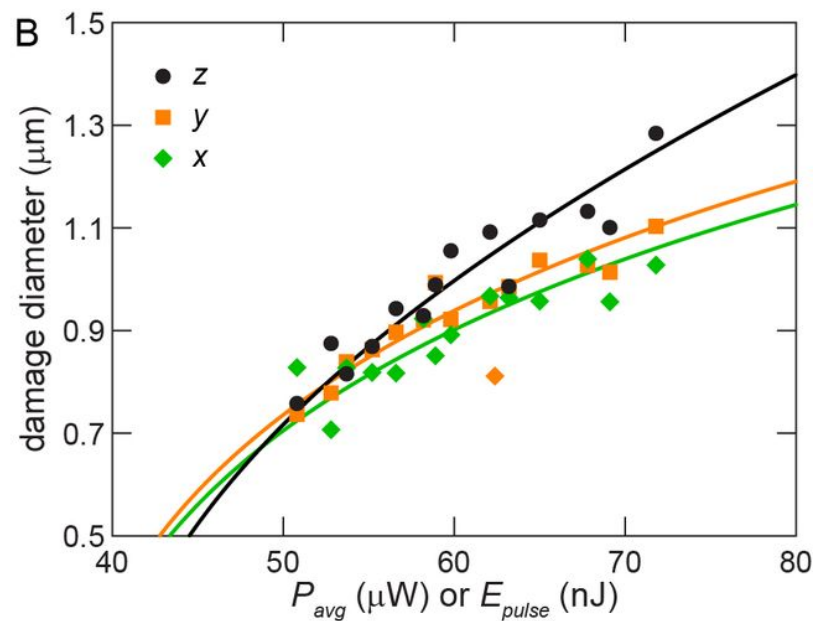
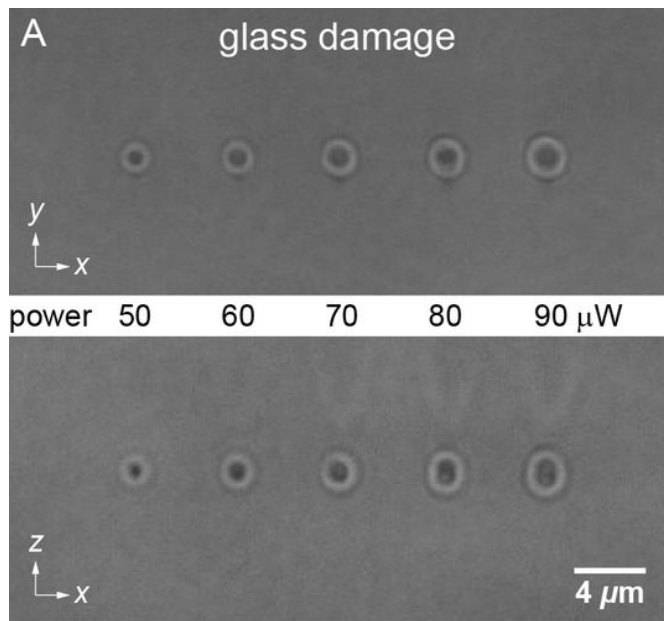


Figure 2

Glass damage spots match theoretical predictions. (a) Transverse and axial plane images of glass damage by focused laser pulses of 50-90 mW. (b) Damage spot measurements in x (diamond), y (square), and z (circle) directions. Green and orange curves plot Eq. 1 with best fit w_0 and I_{th} . Black curve plots Eq. 2 with best fit z_0 and I_{th} .

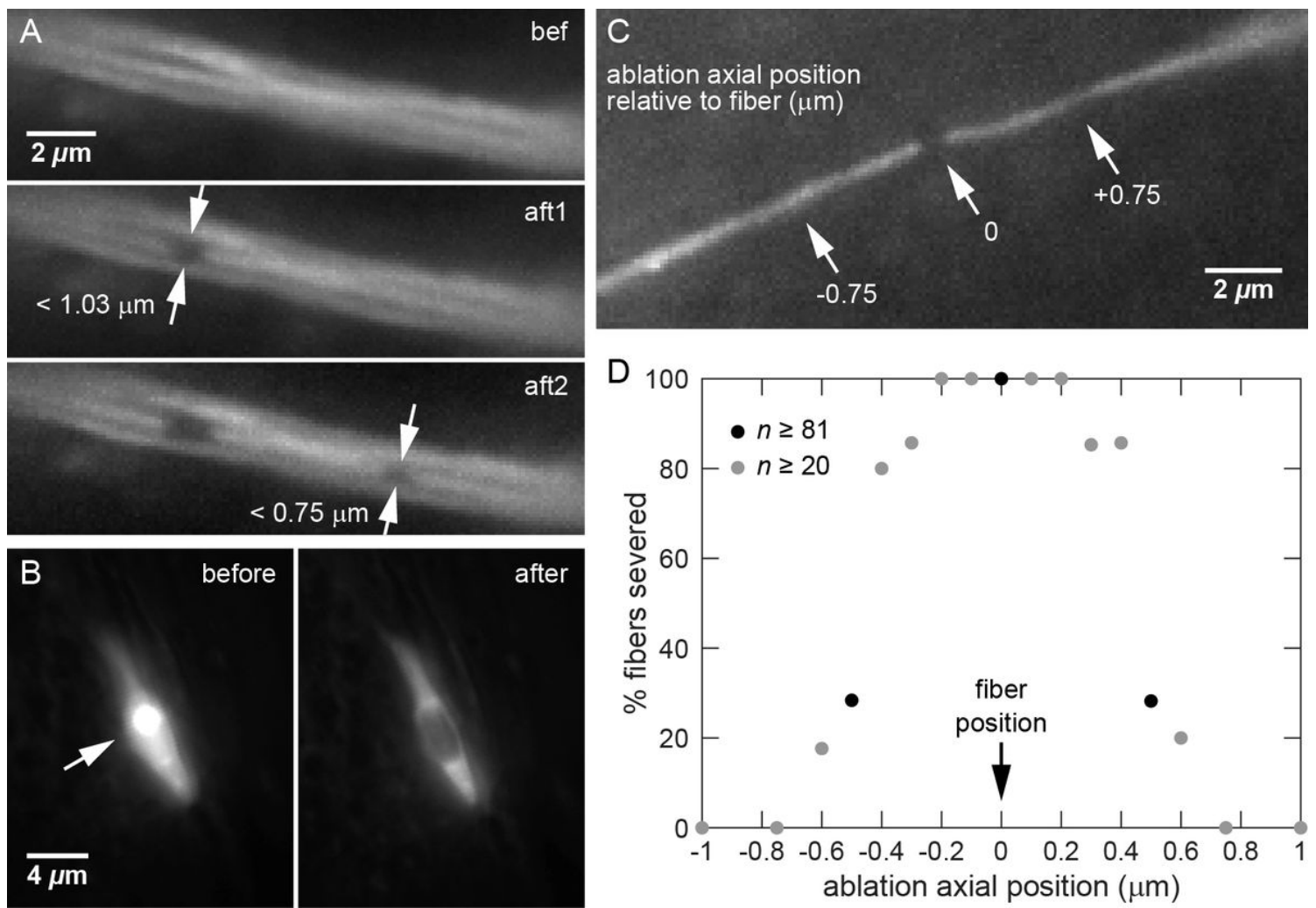


Figure 3

Characterization of *in vivo* laser surgery. (a) Individual neuronal fibers in tight bundle before, after 1st ablation, after 2nd ablation. Images indicate submicrometer transverse resolution of laser surgery. (b) Ablation and photobleaching of nucleus but not cytoplasm shows persistence of nuclear membrane, suggesting axial resolution well below 2 μm . (c) Fiber severed by ablation directly at its axial position but spared by ablation 0.75 mm above or below fiber. (d) Percentage of fibers severed by ablation at various axial positions relative to the fiber. Results indicate submicrometer axial resolution of laser surgery.

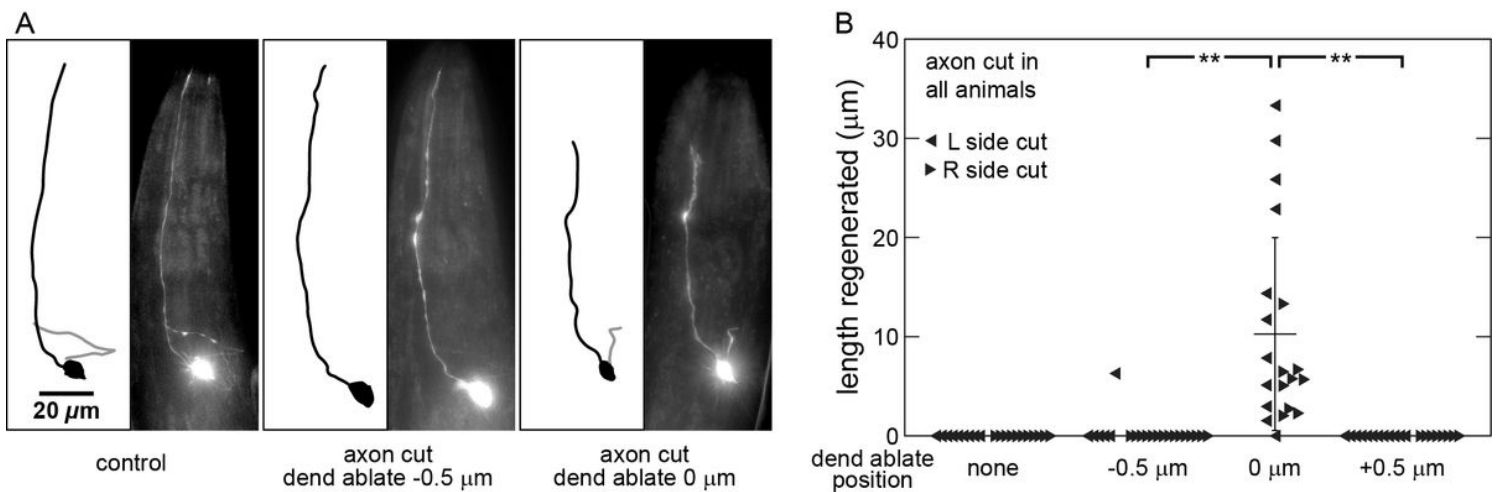


Figure 4

Regeneration assay confirms submicrometer resolution of laser surgery. (a) Line drawings and fluorescent images of ASJ neuron. Control (left) neuron with intact dendrite (black) and axon (gray). Non-control images taken 2 days after surgery: Postsurgery neuron (middle) with cut axon and ablation 0.5 μm below dendrite. Axon has decayed away. Postsurgery neuron (right) with regenerated axon and dendrite ablated directly at its axial position. (b) Length regenerated for each axon cut. Significant regeneration only occurs when dendrites are ablated directly at their axial position; Average and standard deviation indicated by bars. Triangles pointed in direction of side cut. ** $p < 0.0005$.

Supplementary Files

This is a list of supplementary files associated with this preprint. Click to download.

- [Wangetal.SupplementaryInformation20210411.docx](#)